

Supporting Information
of

**Synergistic 1T/2H-MoS₂ Hybrid Phases Enable Exceptional Aluminum-Ion
Battery Performance with High Capacity and Stability**

Seohyeon Yeo^{a,‡}, Moonso Kim^{a,b,‡}, Changhoon Heo^c, Yunji Jeong^a, and Gibaek Lee^{a,*}

^aSchool of Chemical Engineering, Yeungnam University, 38541 Gyeongsan, Republic of Korea

^bSchool of Advanced Materials and Electrical Engineering, Gyeongbuk National University, 36729 Andong, Republic of Korea

^cAI & Robotics Convergence R&D Laboratories, POSCO Holdings, 06194, Seoul, Republic of Korea

[‡]These authors contributed equally to this work.

***Corresponding authors**

To whom correspondence should be addressed.

E-mail: gibaek@ynu.ac.kr (Prof. Gibaek Lee)

Tel.: +82-53-810-2527

Fax: +82-53-810-4631

Index

1. Experimental details

1.1 Preparation of 1T/2H-MoS ₂ and 2H-MoS ₂	S1
1.2 Characterization	S1
1.3 Electrochemical measurement	S1
1.4 DFT calculation	S1

2. Supporting information

Figure S1	S3
Figure S2	S4
Figure S3	S5
Figure S4	S6
Figure S5	S7
Table S1	S8
Figure S6	S9
Figure S7	S10
Figure S8	S11
Figure S9	S12
Figure S10	S13
Figure S11	S14
Figure S12	S15
Table S2	S16
Table S3	S17
Figure S13	S18
Figure S14	S19
Figure S15	S20
Table S4	S21

2. References	S22
----------------------	------------

1. Experimental details

1.1. Preparation of 1T/2H-MoS₂ and 2H-MoS₂

1T/2H-MoS₂ was synthesized via a one-step solvothermal method. MoO₃ (144 mg, Sigma Aldrich), thioacetamide (168 mg, Sigma Aldrich), and urea (1.2 g, Sigma-Aldrich) were dissolved in 80 mL of ethanol and stirred for 4 h. The mixture was transferred to a Teflon-lined stainless-steel autoclave and heated at 200 °C for 16 h in a muffle furnace. After the reaction, the autoclave was rapidly cooled, and the product was washed multiple times with deionized (DI) water and dried at 40 °C under vacuum for 10 h. For 2H-MoS₂, the same procedure was followed using DI water as the solvent and a reaction temperature of 240 °C.

1.2. Characterization

Morphological analysis was conducted using field-emission scanning electron microscopy (FE-SEM, S-4800, HITACHI) and field-emission transmission electron microscopy (FE-TEM, Tecnai G2 F20 S-TWIN, FEI). Atomic alignment was examined using aberration-corrected high-angle annular dark field scanning transmission electron microscopy (ABF-STEM, ARM 200F, JEOL, Japan) equipped with a spherical aberration corrector (ASCOR, CEOS, GmbH, Germany) at Materials Imaging & Analysis Center of POSTECH in South Korea. Compositional and phase analyses were performed using X-ray diffraction (XRD, DIATOME) with a Cu K α source and micro-Raman spectrophotometer (XploRA, Horiba) with a 532 nm Ar⁺ laser. The 1T and 2H phase ratios of Mo-S were determined via X-ray photoelectron spectroscopy (XPS, K-Alpha, Thermo Scientific) using an Al K α source at the Core Research Support Center for Natural Products and Medical Materials at Yeungnam University.

1.3. Electrochemical measurement

Active material, polyvinylidene fluoride (PVDF) binder, and Super P conductive agent were mixed in a 7:2:1 weight ratio in N-methyl-2-pyrrolidone (NMP) to form a homogeneous slurry. The slurry was coated onto a 16-mm molybdenum substrate (current collector) and dried at 80 °C under a vacuum oven for 12 h. The average loading mass of active materials is around 0.6 mg cm⁻². Swagelok cells were assembled in an argon-filled glovebox to prevent ionic liquid oxidation. The cells used an ionic liquid electrolyte composed of 1-ethyl-3-methylimidazolium chloride and aluminum chloride (AlCl₃/[EMIm]Cl) in a 1.3:1 molar ratio with aluminum foil as the anode and a glass microfiber filter (Whatman) as separators. Cyclic voltammetry (CV) was performed in the range of 0.1-1.9 V (vs. Al/Al³⁺) at 0.5 mV s⁻¹ and electrochemical impedance spectroscopy (EIS, ZIVE SP1, IVIUM Technologies) was conducted over a frequency range of 0.1-10 kHz with a 5 mV amplitude.

1.4. Density Functional Theory (DFT) calculation

All DFT calculations were performed using the plane-wave basis projector augmented wave (PAW) from the Quantum Espresso [S1-S3]. The electron exchange-correlation interactions were represented

by the Perdew-burke-Ernzerhof (PBE) pseudopotentials of the generalized gradient approximation (GGA) approach [S4]. Ultrasoft pseudopotentials for all the elements from the standard solid-state pseudopotentials (SSSP) library were used in the calculations [S5]. The wave function cut-off energy was set to 50 Ry and density cut-off energy was set to 500Ry. The Brillouin zone was modeled by the Monkhorst-Pack special k-point mesh with $3 \times 3 \times 1$ gamma-centered grid [S6]. Gaussian smearing of 0.02 Ry instead of Marzari-Vanderbilt smearing was used to determine the electronic occupations around the Fermi level [S7]. The electron convergence threshold was taken to be 10^{-6} Ry, and the Davidson algorithm [S8] was used for the diagonalization of the Kohn-Sham Hamiltonian for the SCF calculations, with a mixing beta of 0.5. Van der Waals' corrections were included in the DFT calculations with Grimme's DFT-D3 scheme [S9]. For the structural relaxations, the Hellmann-Feynman forces were minimized below 0.01 eV/\AA , employing the Broyden-Fletcher-Goldfarb-Shanno (BFGS) algorithm [S10].

The intercalation energy (ΔE_b) was calculated as

$$\Delta E_b = E_{tot}(\text{Al}^{3+}/\text{MoS}_2) - E_{tot}(\text{MoS}_2) - E_{tot}(\text{Al}^{3+})$$

Where $E_{tot}(\text{Al}^{3+}/\text{MoS}_2)$, $E_{tot}(\text{MoS}_2)$, and $E_{tot}(\text{Al}^{3+})$ are the total energies of Al^{3+} intercalated MoS_2 , the corresponding MoS_2 bulk structure with and the Al^{3+} ion structure. The most negative binding energy shows the most favorable exothermic interaction of Al^{3+} in MoS_2 .

The NEB approach was adopted to obtain the diffusion energy profiles using five images between two stable adsorption structures [S11-S13]. The NEB algorithm necessitates the input of the initial and final states of the diffusion process. From these states, it generates several intermediate states, referred to as images, through linear interpolation. The minimum energy path (MEP) that connects these initial and final states is subsequently determined by concurrently minimizing the atomic forces on all images while applying a harmonic coupling between neighboring images.

2. Supporting information

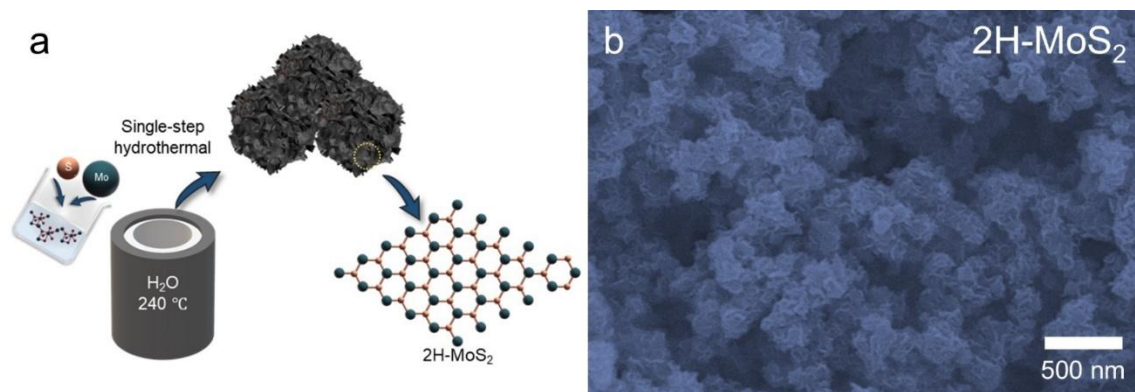


Figure S1. (a) Schematic illustration depicting the synthesis procedure of 2H-MoS₂. (b) SEM image of 2H-MoS₂.

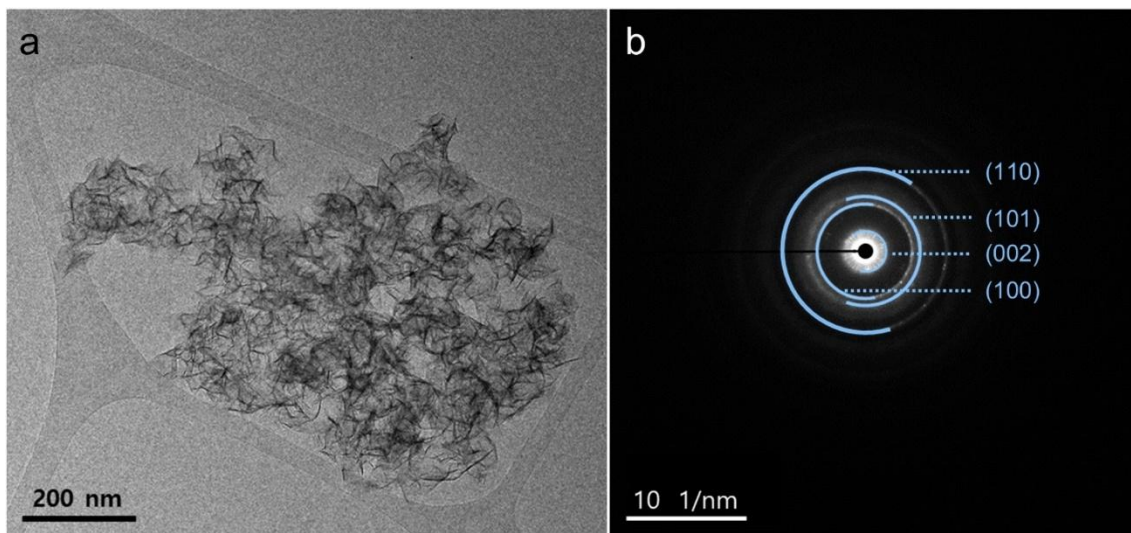


Figure S2. (a) TEM image and (b) SAED pattern of 2H-MoS₂.

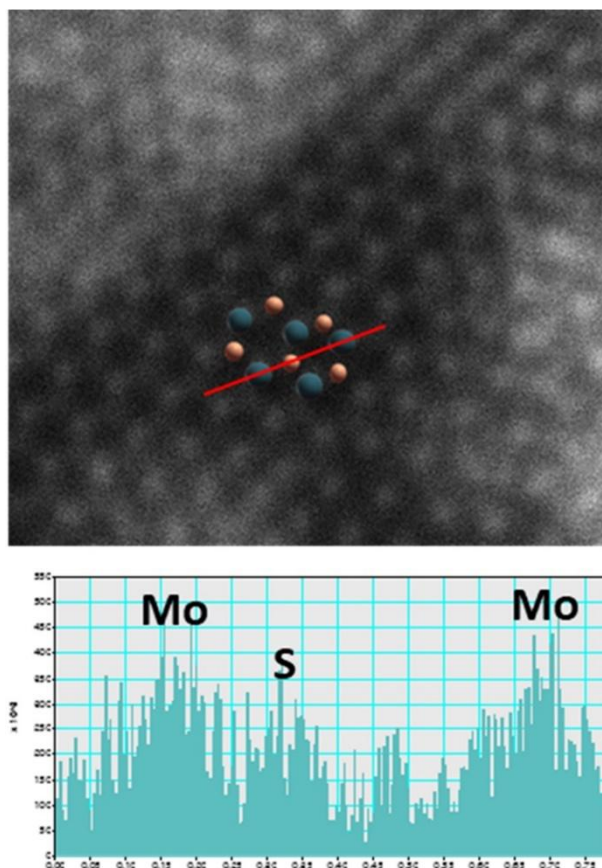


Figure S3. STEM and corresponding line scan analysis of atomic distances in 2H-MoS₂.

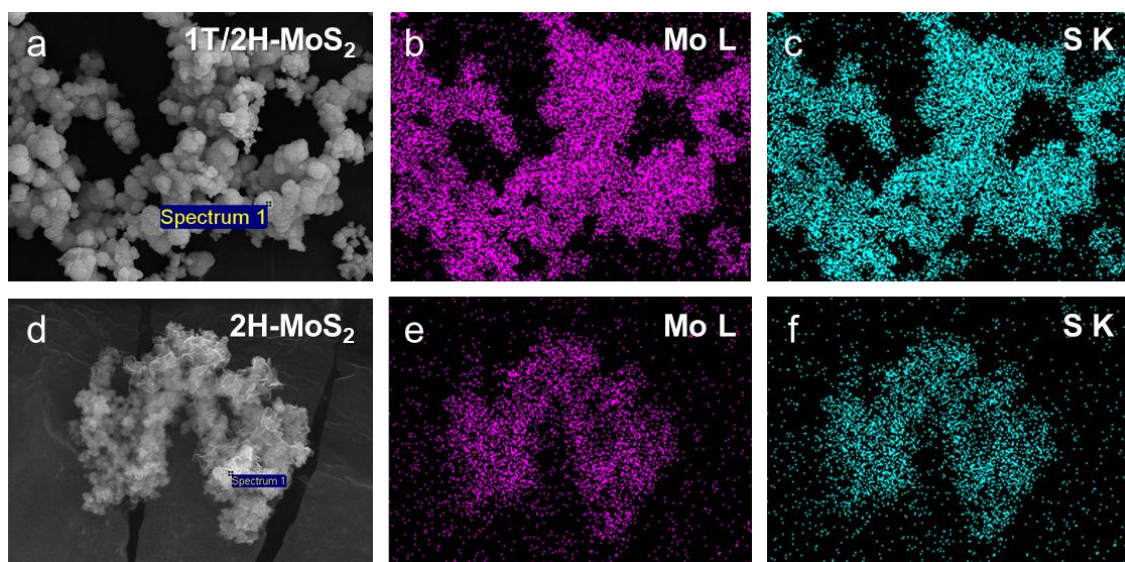


Figure S4. SEM-EDS mapping images of (a-c) 1T/2H-MoS₂ and (d-f) 2H-MoS₂.

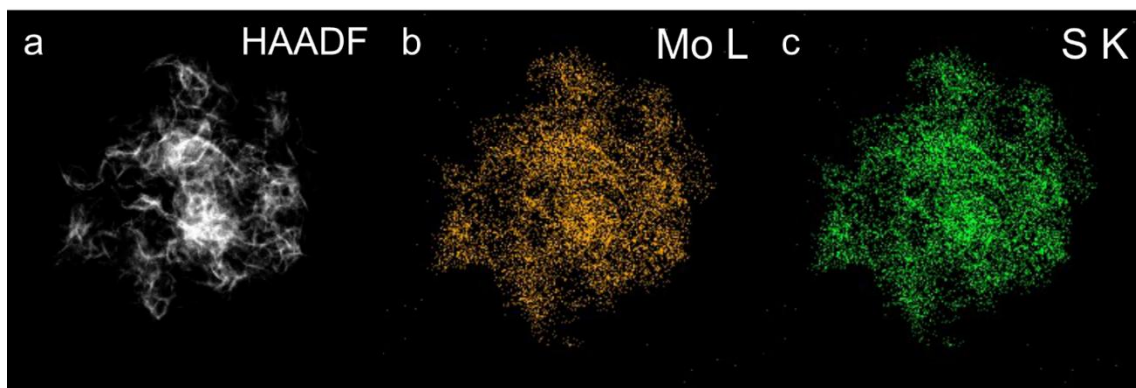


Figure S5. TEM-EDS mapping images of 2H-MoS₂.

Table S1. Comparison of Mo and S elements concentrations determined by TEM-EDS.

	Mo L	S K	Mo:S
1T/2H-MoS₂	34.28 at%	65.72 at%	1:1.9
2H-MoS₂	32.06 at%	67.94 at%	1:2.1

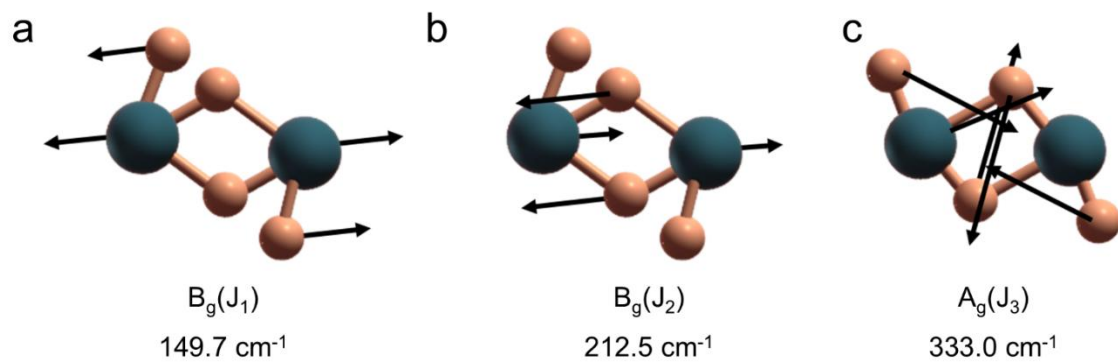


Figure S6. Vibration modes observed in 1T/2H-MoS₂. (a) J₁ mode, (b) J₂ mode, and (c) J₃ mode associated with the 1T phase.

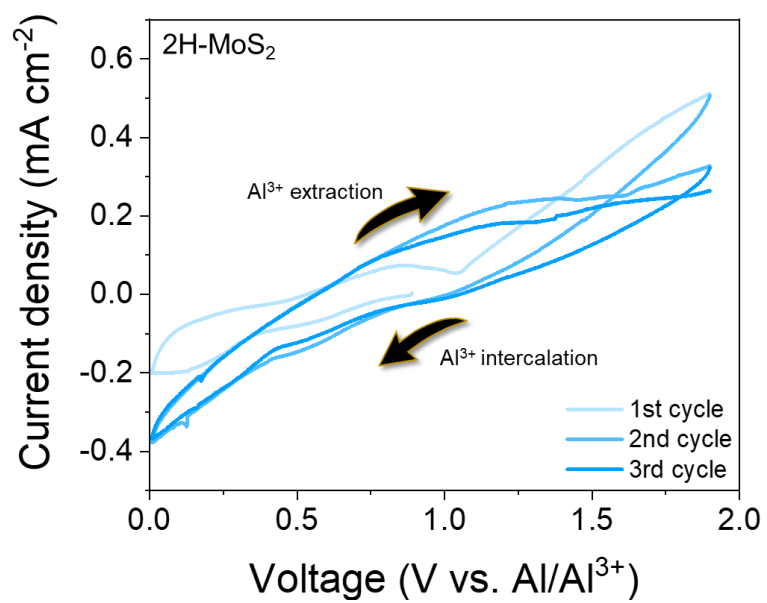


Figure S7. Cyclic voltammetry curve of 2H-MoS₂.

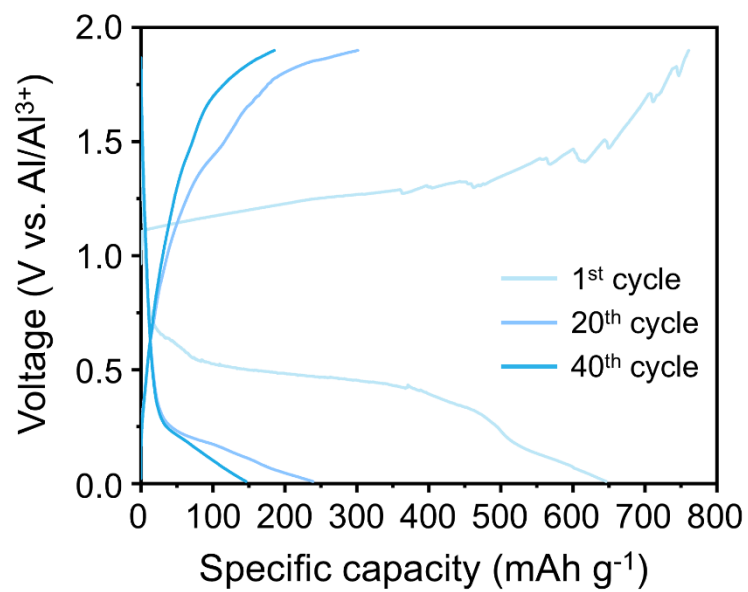


Figure S8. Galvanostatic charge/discharge profiles of 2H-MoS₂ at different cycles.

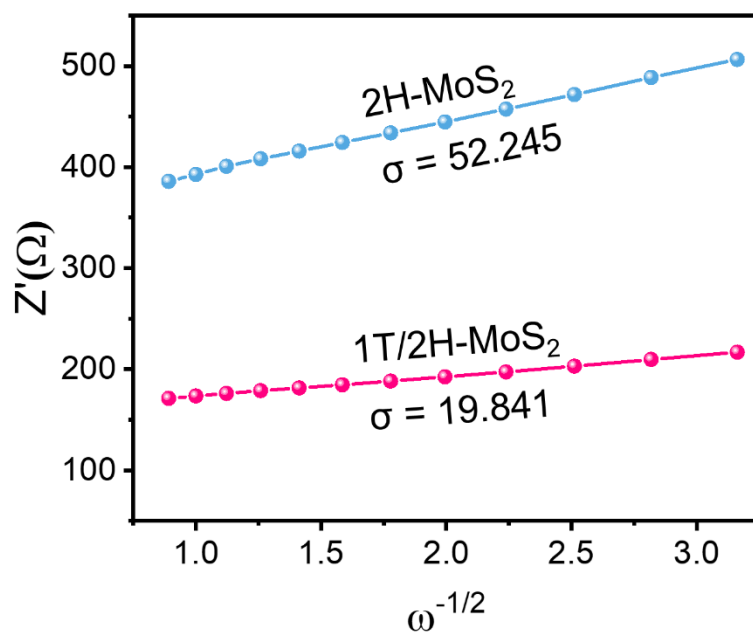


Figure S9. Warburg factor correlations of 1T/2H-MoS₂ and 2H-MoS₂ after 100 cycles.

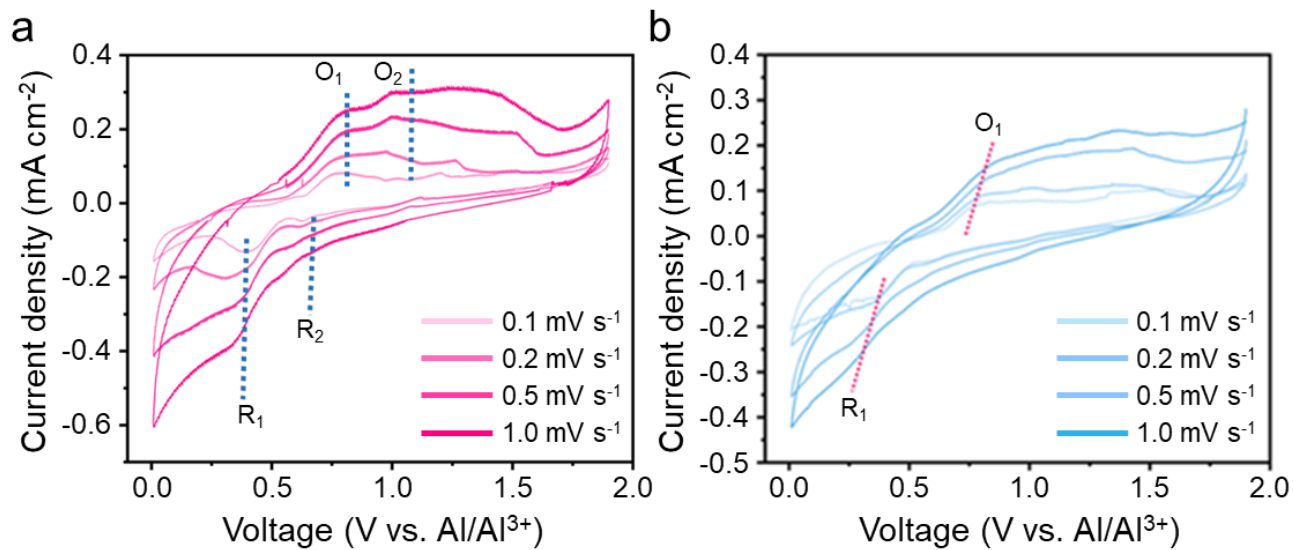


Figure S10. CV curves of (a) 1T/2H-MoS₂ and (b) 2H-MoS₂ with various scan rates.

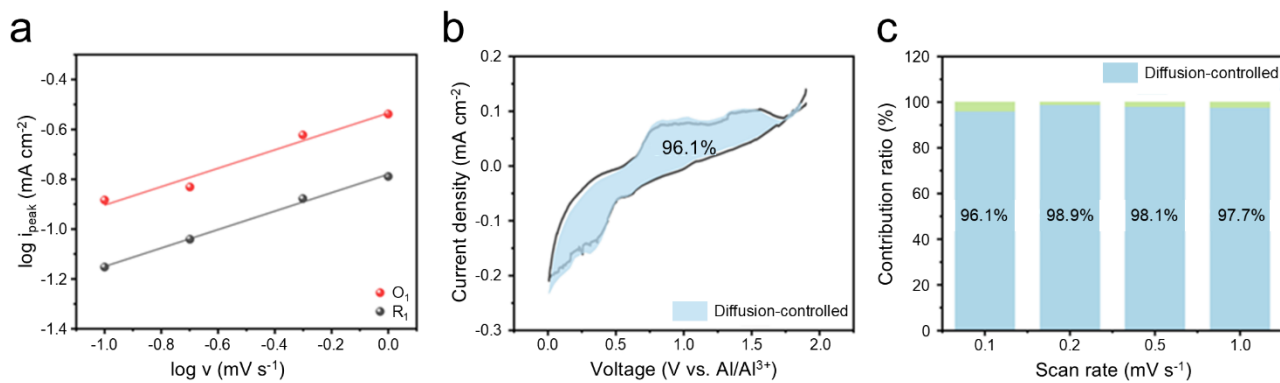


Figure S11. (a) Randles-Sevchik plots, (b) CV with diffusion-controlled contributions, and (c) capacitive-diffusion distribution histograms for 2H-MoS₂.

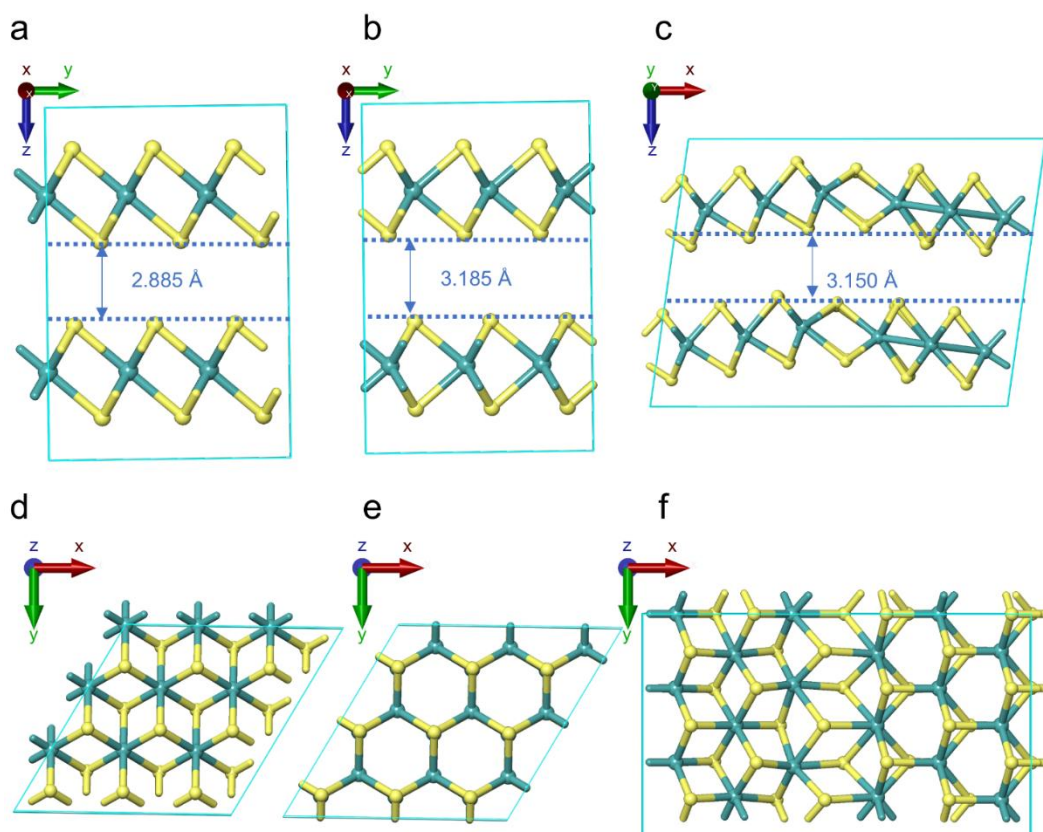


Figure S12. Structural representations of MoS₂ phases. (a-c) Side-view illustrating the layered stacking arrangements of 1T, 2H, and 1T/2H heterostructures. (d-f) Top-view highlighting the atomic configurations and symmetry of 1T, 2H, and 1T/2H heterostructures.

Table S2. The calculated lattice parameters of MoS₂ series.

State	Materials	Lattice size parameters (Supercell, Å)			Lattice angle parameters (°)		
		<i>x</i>	<i>y</i>	<i>z</i>	α	β	γ
Bare MoS ₂ series	1T-MoS ₂	9.55226	9.5443359	12.076364	90	90	120
	2H-MoS ₂	9.49606	9.49606	12.62696	90	90	120
	1T/2H- MoS ₂	16.706675	9.527807	12.677828	90	98.156	90.002

Table S3. Lattice angle parameters of MoS₂ series whether Al³⁺ charged/discharged.

State	Materials	Lattice angle parameters		
		α	β	γ
Al ³⁺ extracted (charged 1.9 V)	1T-MoS ₂	90	90	120
	2H-MoS ₂	90	90	120
	1T/2H-MoS ₂	90	98.156	90.002
Al ³⁺ intercalated (discharged 0.01 V)	1T-MoS ₂	89.526	90.154	119.968
	2H-MoS ₂	90	90	120
	1T/2H-MoS ₂	90.143	81.877	89.991

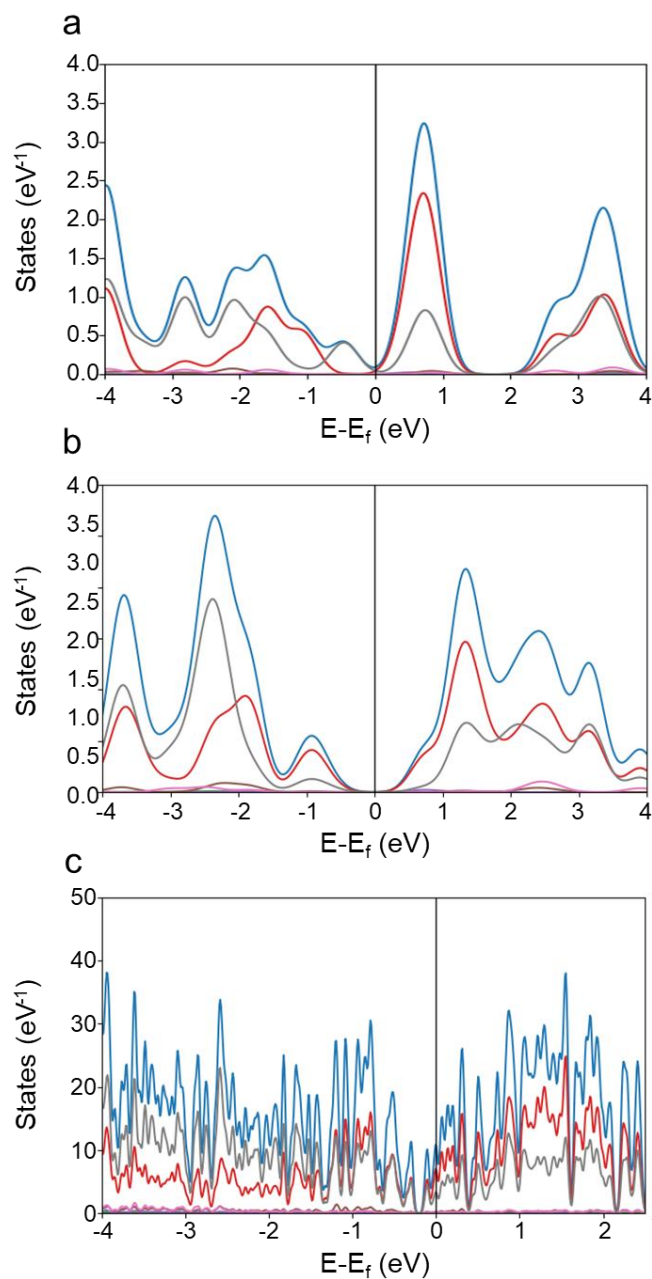


Figure S13. Total and orbital-projected density of states (DOS) for (a) unfunctionalized 1T-MoS₂, (b) 2H-MoS₂ in its primitive cell, and (c) 1T/2H-MoS₂ in its conventional cell. The Fermi level is marked by a solid line and calibrated to zero energy.

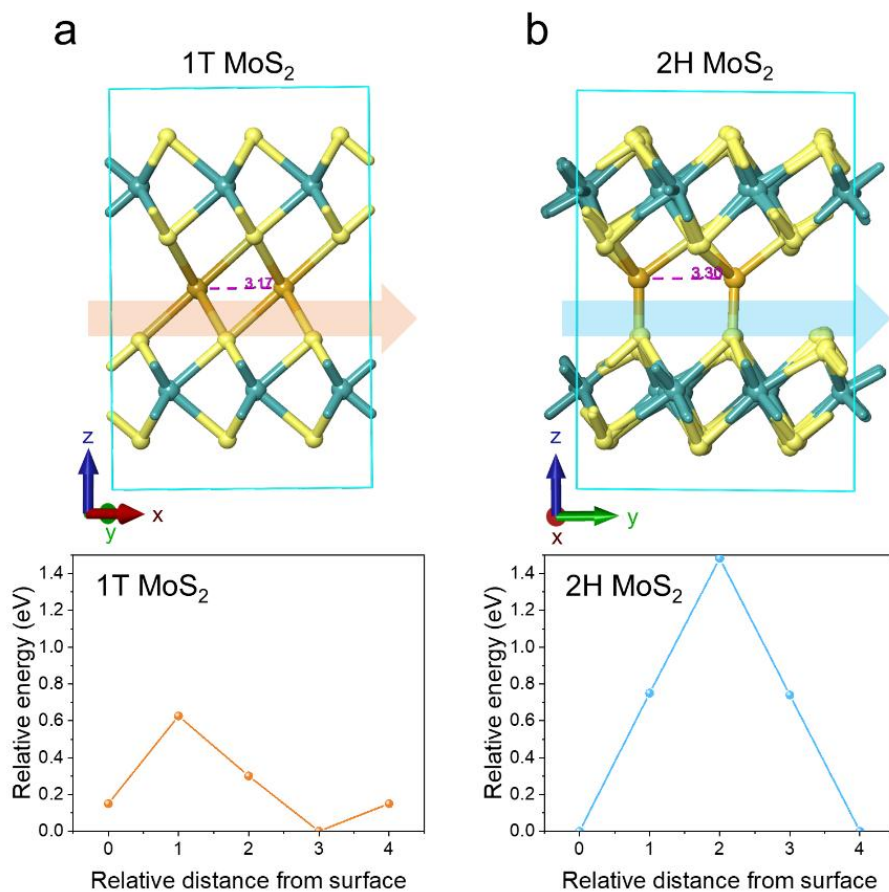


Figure S14. Computed energy barriers for Al^{3+} ion diffusion in (a) 1T-MoS₂ and (b) 2H-MoS₂. The graphs provide diffusion pathways and associated activation energies for Al^{3+} migration between adjacent sites.

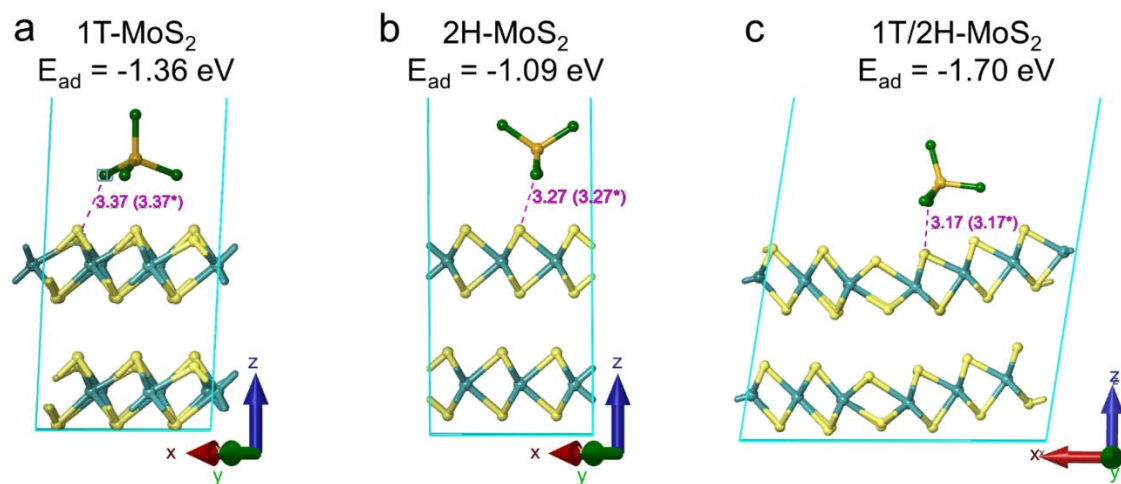


Figure S15. Adsorption configurations of AlCl₄⁻ on double-layered MoS₂ phases. (a) 1T-MoS₂, (b) 2H-MoS₂, and (c) 1T/2H-MoS₂.

Table S4. Comparative summary of aluminum ion battery performance of MoS₂-based cathode materials reported in literature.

Materials	Specific capacity (mAh g ⁻¹)	Potential range (V)	Current density (A g ⁻¹)	Cyclability (n)	Electrolyte	Reference
1T/2H-MoS₂ nanoflower	187	0.01 – 1.9 V	0.2 A g⁻¹	100	1.3:1 AlCl₃:EMImCl	This study
2H-MoS ₂ nanosheet	750	0.65 – 1.9 V	5 A g ⁻¹	200	10:1 AlCl ₃ :H ₂ O Water-in-Salt	[S14]
2H-MoS ₂ nanosheet	66.7	0.5 – 2.0 V	0.04 A g ⁻¹	100	1.3:1 AlCl ₃ :EMImCl	[S15]
MoS ₂ -rGO composite	150.2	0.1 – 2.3 V	1.0 A g ⁻¹	100	1.3:1 AlCl ₃ :EMImCl	[S16]
MoS ₂ -MXene composite	166	0.1 – 1.8 V	1.0 A g ⁻¹	60	1.3:1 AlCl ₃ :EMImCl	[S17]
FeSe ₂ /MoS ₂	116	0.01 – 1.8 V	1.0 A g ⁻¹	140	1.1:1 AlCl ₃ :EMImCl	[S18]
MoS ₂ /N-doped carbon	127.5	0 – 1.8 V	1.0 A g ⁻¹	1700	1.3:1 AlCl ₃ :EMImCl	[S19]

References

- [S1] P. E. Blöchl, *Phys. Rev. B*, 1994, **50**, 17953- 17979.
- [S2] P. Giannozzi, S. Baroni, N. Bonini, M. Calandra, R. Car, C. Cavazzoni, D. Ceresoli, G. L. Chiarotti, M. Cococcioni, I. Dabo, A. Dal Corso, S. Fabris, G. Fratesi, S. de Gironcoli, R. Gebauer, U. Gerstmann, C. Gougoussis, A. Kokalj, M. Lazzeri, L. Martin-Samos, N. Marzari, F. Mauri, R. Mazzarello, S. Paolini, A. Pasquarello, L. Paulatto, C. Sbraccia, S. Scandolo, G. Sciauzero, A. P. Seitsonen, A. Smogunov, P. Umari, R. M. Wentzcovitch, *J. Phys. Condens. Matter*, 2009, **21**, 395502.
- [S3] P. Giannozzi, O. Baseggio, P. Bonfà, D. Brunato, R. Car, I. Carnimeo, C. Cavazzoni, S. de Gironcoli, P. Delugas, F. Ferrari Ruffino, A. Ferretti, N. Marzari, I. Timrov, A. Urru, S. Baroni, *J. Chem. Phys.*, 2020, **152**, 154105.
- [S4] J. P. Perdew, K. Burke, M. Ernzerhof, *Phys. Rev. Lett.*, 1996, **77**, 3865-3868.
- [S5] G. Prandini, A. Marrazzo, I. E. Castelli, N. Mounet, N. Marzari, *NPJ Comput. Mater.*, 2018, **4**, 72.
- [S6] H. J. Monkhorst, J. D. Pack, *Phys. Rev. B*, 1976, **13**, 5188-5192.
- [S7] N. Marzari, D. Vanderbilt, A. De Vita, M. Payne, *Phys. Rev. Lett.*, 1999, **82**, 3296-3299
- [S8] E. R. Davidson, *Methods in Computational Molecular Physics* NATO Advanced Study Institute, Series C, Plenum, New York (1983)
- [S9] S. Grimme, *J. Comput. Chem.*, 2006, **27**, 1787-1799.
- [S10] J. D. Head, M. C. Zerner, *Chem. Phys. Lett.*, 1985, **122**, 264-270.
- [S11] D. Sheppard, P. Xiao, W. Chemelewski, D. D. Johnson, G. Henkelman, *J. Chem. Phys.*, 2012, **136**, 074103.
- [S12] D. Sheppard, R. Terrell, G. Henkelman, *J. Chem. Phys.*, 2008, **128**, 134106.
- [S13] D. Sheppard, G. Henkelman, *J. Chem. Phys.*, 2011, **32**, 1769-1771.
- [S14] Z. Li, B. Niu, J. Liu, J. Li, F. Kang, *ACS Appl. Mater. Interfaces*, 2018, **10**, 9451-9459.
- [S15] W. Pan, Y. Zhang, K. W. Leong, Y. Zhang, J. Mao, Y. Wang, X. Zhao, S. Luo, D. Y. C. Leung, *Small Methods*, 2024, **8**, 2301206.
- [S16] B. Tan, S. Han, W. Luo, Z. Chao, J. Fan, M. Wang, *J. Alloys Compd.*, 2020, **841**, 155732.
- [S17] B. Tan, T. Lu, W. Luo, Z. Chao, R. Dong, J. Fan, *Energy & Fuels*, 2021, **35**, 12666-12670.
- [S18] B. Zhang, R. Kang, W. Zhou, Y. Du, H. Wang, J. Wan, J. Zhang, *ACS Appl. Energy Mater.*, 2023, **6**, 3366-3373.
- [S19] S. Guo, H. Yang, M. Liu, X. Feng, H. Xu, Y. Bai, C. Wu, *ACS Appl. Energy Mater.*, 2021, **4**, 7064-7072.